Received September 5, 2020, accepted September 23, 2020, date of publication September 29, 2020,
date of current version October 14, 2020.

Digital Object Identifier 10.1109/ACCESS.2020.3027537

Application of the Mixing Theory in the Design of a High-Performance Dielectric Substrate for Microwave and Mm-Wave Systems

SYED SHAHAN JEHANGIR[1,2], ZEESHAN QAMAR[2], (Member, IEEE), NAFATI ABOSERWAL[1,2], (Member, IEEE), AND JORGE L. SALAZAR-CERRENO[1,2], (Senior Member, IEEE)

[1]School of Electrical and Computer Engineering, The University of Oklahoma, Norman, OK 73019, USA
[2]Advanced Radar Research Center (ARRC), The University of Oklahoma, Norman, OK 73019, USA

Corresponding author: Jorge L. Salazar-Cerreno (salazar@ou.edu)

This work was partially supported by the U.S. Department of Defense, Office of Naval Research (DOD-ONR) under Grant N00014-18-1-2035, and in part by the Office of Navy Research (ONR) under Grant 1532140.

ABSTRACT This paper presents the design and synthesis of a low-loss substrate with low effective permittivity (ε_{eff}) for microwave and mm-Wave applications. The proposed design is based on the two-phase Maxwell Garnet mixing theory, where the ε_{eff} of the RF substrate can be synthesized depending on the geometry and the permittivity of mixing particles and the permittivity of the host material. A comprehensive review and error analysis of the most common mixing techniques are conducted to guarantee an accurate design for high-performance RF substrates. Several analyses based on the geometries of various particles are carried out to identify the most accurate mixing model used in the design of the proposed substrate. The effects of the direction of excitation as well as the polarization of the incident field on the ε_{eff} of the anisotropic particle are analyzed and discussed. The proposed method enables the use of existing high-performance materials that do not necessarily provide a low dielectric constant and low loss tangent. For mm-Wave antenna applications, materials with a dielectric constant of 2–4, and loss tangent of less than 0.002 are desirable to maximize gain and radiation efficiency. Commercial RF substrates can satisfy those requirements, however limited thermal expansion coefficient and lamination difficulties increase the cost significantly. The proposed method enables the use of inexpensive materials that provide excellent thermal properties and great compatibility with a multi-layer fabrication process with desirable ε_{eff} and loss tangent. For validation of the analysis, samples are fabricated and tested in the microwave frequency (S-band) at 3.5 GHz as well as in the mm-Wave frequency (W-band) at 77 GHz. Measured results show a reduction of 45% in the ε_{eff} and 38% in the loss tangent values in the S-band, and 32% and 72% reduction in ε_{eff} and tanδ, respectively, in the mm-Wave frequency band. The measured results are in excellent agreement with the simulation and calculated results.

INDEX TERMS Anisotropic, conventional, complementary, effective permittivity, isotropic, low loss-tangent, Maxwell Garnett mixing theory, polarization, dielectric constant.

I. INTRODUCTION

A complete understanding of the propagation of electromagnetic waves inside the dielectric material is of great importance in the modern applications of material design, remote sensing, aerospace, lens manufacturing, electromagnetic absorbers, carbon nanotubes, and polymers, etc. [1]–[3]. The dielectric properties of the material depend on the internal structure of the particles inside, particles shape, and the fractional volume (f). Several analytical models or mixing rules exist in the literature that have studied these properties and simplified modeling of the complex fields generated in the particles inside the host material. Material mixing rules are a set of algebraic formulations intended to calculate the effective permittivity (ε_{eff}) of the inclusions or particles inside the mixture based on the individual permittivities of

The associate editor coordinating the review of this manuscript and approving it for publication was Jenny Mahoney.

This work is licensed under a Creative Commons Attribution 4.0 License. For more information, see https://creativecommons.org/licenses/by/4.0/

the particles as well as their fractional volumes. These mixing rules differ based on several factors such as structure or geometry of the particle (sphere, elliptical, disc, cubic, cylindrical, rod, needle-like, or any random shape) and their distribution inside the host material (aligned or randomly distributed). The geometry of the particles inside the host material determines the isotropic or anisotropic properties of the material. For instance, a spherical inclusion is considered isotropic as the ε_{eff} evaluated in x-, y-, and z-directions remains the same. This is because, the sphere is symmetric due to which the induced electric field inside the particle is uniform, thus making the polarizability (α) as a scalar quantity. On the other hand, in the case of anisotropic particles, ε_{eff} is a tensor and is evaluated in each direction of the applied electric field. Generally, for antennas or other microwave devices, ε_{eff} is evaluated in the z-direction. However, characterization of the material for its ε_{eff} in the x- or y-directions can be important in applications such as leaky wave antennas or in the devices where the surface waves are critical to the performance of the system.

Several works on controlling the permittivity of the material are presented for various applications such as multi-band arrays and integrated systems [4]–[9]. The concept of using perforations to control the effective permittivity for the substrate integrated image guide (SIIG) was first reported in [4], [5]. Cylindrical metallic particles were embedded in the host medium in [7] to change the overall permittivity of the substrate material and to obtain frequency tuning for a microstrip patch antenna. In [8], linearly tapered slot antennas were presented for 30 and 94 GHz bands on the synthesized low-permittivity of the perforated substrate. A leaky-wave antenna based on a dielectric layer with periodic perforations covering $96-108$ GHz frequency band was presented in [9].

Choosing the right printed circuit board (PCB) material is significantly important for both microwave and mm-Wave frequency bands. The main losses associated with the PCB materials are: radiation losses, dielectric, conductor, and surface-wave losses. None of these losses can be ignored at mm-Wave frequencies, specifically the conductor losses, which become significant at mm-Wave frequencies. To achieve optimum performance from a PCB at any frequency of operation, several factors are evaluated: dielectric constant (ε_r), loss tangent (tanδ), copper roughness, coefficient of thermal expansion (CTE), moisture absorption, and material thickness [10]. However, at high frequencies, some of these factors become more critical such as ε_r, tanδ, copper roughness, and material thickness [11].

At microwave frequencies, high ε_r material ($8-500$) can be used to achieve miniaturization of the circuit [12]. However, at mm-Wave frequencies, low ε_r material ($2-4$) is preferred in order to reduce losses in the material (tanδ). The conductor losses, which are either due to the material's surface finishing or copper roughness, become critical at mm-Wave frequencies. The losses from the copper roughness are directly related to the frequency of operation through the skin depth. At higher frequencies, these losses are significant because the value of the skin depth becomes smaller than the copper roughness. Moreover, the thickness of the PCB is also a very important factor of consideration during material selection. For instance, at higher frequencies, thick materials are prone to significant radiation losses as compared to the thin materials. But at the same time, thin materials are dominated by the conductor losses. Therefore, choosing a thin material with lower copper surface roughness is highly recommended for use at mm-Wave frequencies over a thick material with low conductor losses but higher radiation losses [11].

As applications move up in frequency, affordable and high-performance substrates are required. In military applications, polytetrafluoroethylene (PTFE) substrates had been considered as one of the best materials for RF applications. Teflon or PTF-based substrates provide very low tanδ (0.0018 at 10 GHz) and offer great chemical resistant properties, small water absorption, and high-temperature resistance [13]. However, when the applications require high-performance substrates such as PTFE, those substrates present limitations in cost. For example, PTFE is ten times the price of epoxy glass (FR4), and five times the price of ceramic-based materials. In addition, PTFE requires extra preparation for good adhesion for multi-layer PCB process. Moreover, conventional PTFE substrates are soft and CTE of the conventional PTFE substrates is very high (180 to 205 ppm/°C) [13]. The proposed method enables the use of the existing inexpensive materials that provide excellent thermal properties and great compatibility with a multi-layer fabrication process to obtain high RF-performance in terms of desirable ε_{eff} and tanδ values for antenna applications.

In this paper, a proposed method based on Maxwell Garnett mixing theory is used to obtain a low-cost material with high RF performance, from existing high thermally stable and compatible materials. A complete set of design equations for finding desirable ε_{eff} of both isotropic and anisotropic particles is presented. For anisotropic cylindrical particle, several ε_{eff} models are analyzed and compared for its performance with the simulation results. The permittivity analysis for both isotropic and anisotropic cases is thoroughly studied including the effects of the direction of excitation: x-, y-, and z-directions. Moreover, the effect of polarization of the incident field on the ε_{eff} is also studied. Detailed material requirements and design procedures are discussed for both microwave and mm-Wave frequencies. The proposed perforated dielectric core material is fabricated and the simulation and measured results are used for validation. An excellent agreement is obtained between the simulation and measured results. For the proof of concept, Rogers 4350B material is loaded with cylindrical air particles and is tested in the microwave S-band. A reduction of 45% in the ε_{eff} and 38% in the loss tangent values were obtained. The results are also validated in the mm-Wave W-band by loading RO3003 with the complementary cylindrical air particles showing a reduction of 32% and 72% in ε_{eff} and tanδ values, respectively.

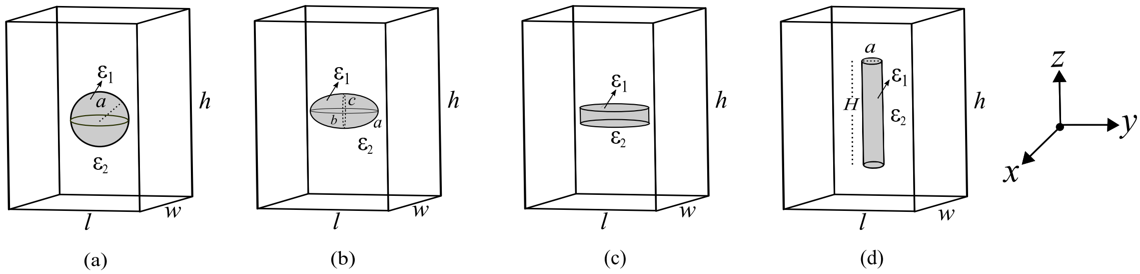

FIGURE 1. Isotropic and anisotropic unit cell geometries used for the mixing technique. (a) Sphere. (b) Ellipsoid. (c) Disc. (d) Cylinder.

II. EFFECTIVE PERMITTIVITY AND MIXING TECHNIQUES

Several dielectric mixing rules have widely been used in literature such as: Maxwell Garnett mixing formula [14], Bruggeman [15], Looyenga [16], Polder–van Santen rule [17], and Lichtenecker mixing formula [18], etc. The most common of all these models is the Maxwell Garnett rule which is in the simplest form and is broadly applicable to a variety of particles. The theoretical background and analytic derivation of the Maxwell Garnett formula are not discussed here, as it is not the focus of this work. However, in this section, the required formulations that can be used for finding the ε_{eff} of any isotropic (sphere, cubic) and anisotropic (cylindrical, disc, elliptical) particles, are presented.

The generic Maxwell Garnett mixing rule having the depolarization information is given by (1) [19].

$$\varepsilon_{eff_j} = \varepsilon_2 \left(1 + \frac{(\varepsilon_1 - \varepsilon_2)f}{\varepsilon_2 + (\varepsilon_1 - \varepsilon_2)(1-f)N_j}\right); j = x, y, z \tag{1}$$

where, ε_1 and ε_2 are the permittivities of the particle and the host material, respectively. f is the fractional volume of the mixing particle, and N_j is the depolarization factor opposing the direction of the applied field.

A. ISOTROPIC PARTICLES

For an isotropic particle, the value of $N_j = 1/3$, where j $= x$, y, and z [19]. An example geometry of the isotropic particle is shown in Fig. 1(a). By replacing the value of $N = 1/3$ in (1), it can be easily shown that the ε_{eff} for an isotropic particle can be calculated from a more common form of Maxwell Garnett mixing formulation given by (2)

$$\varepsilon_{eff} = \epsilon_2 \frac{\varepsilon_1 + 2\varepsilon_2 + 2f(\varepsilon_1 - \varepsilon_2)}{\varepsilon_1 + 2\varepsilon_2 - f(\varepsilon_1 - \varepsilon_2)} \tag{2}$$

B. ANISTROPIC PARTICLES

1) ELLIPSOID PARTICLE

The geometry of an ellipsoid inside a host medium is shown in Fig. 1(b). The depolarization factor N_x can be calculated from (3) [20].

$$N_x = \frac{abc}{2}\int_0^{+\infty} \frac{ds}{(s+a^2)\sqrt{(s+a^2)(s+b^2)(s+c^2)}} \tag{3}$$

where, a, b, and c are the semi-axes of the ellipsoid. N_y and N_z can be calculated by interchanging b and a, and c and a, respectively. Closed-form expressions of (3) can be found in [21]. The depolarization factors of a general ellipsoid can also be found in [22]–[23]. Once the depolarization factors are known, (1) can be used to find the ε_{eff} in any direction.

2) DISC PARTICLE

The unit cell geometry of a disc particle is shown in Fig. 1(c). As the particle is symmetric in x- and y-directions, the permittivity in either x- or y-, and z-directions need to be evaluated. Equations (4) and (5) can be used to find the ε_{eff} in the z- and x- or y-directions, respectively [24].

$$\frac{1}{\varepsilon_{eff_z}} = \frac{f}{\varepsilon_1} + \frac{1-f}{\varepsilon_2} \tag{4}$$

$$\varepsilon_{eff_{xy}} = f\varepsilon_1 + (1-f)\varepsilon_2 \tag{5}$$

3) CYLINDRICAL PARTICLE

The geometry of the unit cell of the cylindrical particle is shown in Fig. 1(d). The formulations for the cylindrical particle which is used in the design of our proposed material are discussed in detail. Unfortunately, the exact analytical models for finding the ε_{eff} of the material consisting of cylindrical particles do not exist. However, very few models discussing the approximate depolarization factor for the cylindrical particle exist, which are discussed in this section. In the following sections, we then compare the performance of these models based on their depolarization factors. We show that after choosing the right depolarization factor, the generic Maxwell Garnett formulation is then applicable to find the ε_{eff} using the cylindrical particle, in any direction (x-, y-, z-) or any polarization ($\parallel$ or $\perp$) of the applied field with an overall error of $\leq 5\%$ in all cases.

The polarizability (α_j) for a cylindrical particle is calculated numerically using method of moments (MoM) [25]–[26]. For the anisotropic particle, α_j for $j = z$ and $j = x$ or y are given by (6) and (7), respectively:

$$\alpha_z \approx 3.8662(\varepsilon_r - 1) \times \frac{\varepsilon_r^3 - 0.0519\varepsilon_r^2 + 0.9427\varepsilon_r + 1.5840}{\varepsilon_r^4 + 3.2226\varepsilon_r^3 - 0.0021\varepsilon_r^2 + 5.3391\varepsilon_r + 3.8662} \tag{6}$$

$$\alpha_{x,y} \approx 3.1691(\varepsilon_r - 1) \times \frac{\varepsilon_r^3 + 2.0283\varepsilon_r^2 + 1.9821\varepsilon_r + 1.5799}{\varepsilon_r^4 + 4.4453\varepsilon_r^3 + 6.2134\varepsilon_r^2 + 6.05\varepsilon_r + 3.1691} \tag{7}$$

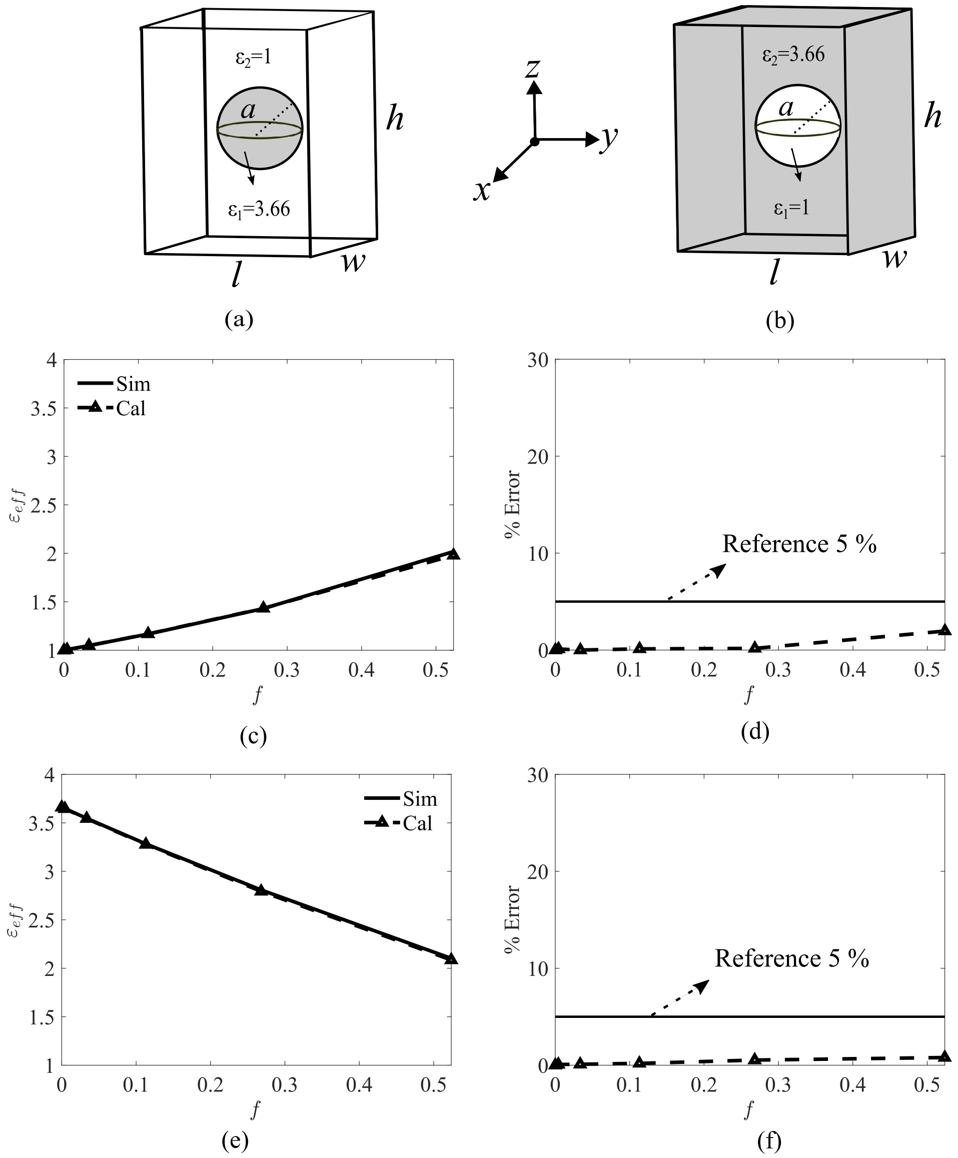

FIGURE 2. **Permittivity analysis for the isotropic spherical particle. (a) Unit cell geometry of the conventional particle. (b) Unit cell geometry of the complementary particle. (c) Simulated and calculated ε_{eff} for the conventional particle as a function of the fractional volume (f). Calculated results use (2) [19]. (d) Permittivity perceptual error (%) for the conventional particle as a function of f. (e) Simulated and calculated ε_{eff} for the complementary particle as a function f. Calculated results use (2) [19]. (f) Permittivity perceptual error (%) for the complementary particle as a function of f.**

where, ε_r is the permittivity of the mixing particle. The depolarization factor N_j can then be found from α_j using (8) [19], which is then substituted in (1) to find the ε_{eff}.

$$\alpha_j = \left(\frac{\varepsilon_2(\varepsilon_1 - \varepsilon_2)f}{\varepsilon_2 + (\varepsilon_1 - \varepsilon_2)N_j} \right); j = x, y, z \tag{8}$$

The second formulation, known as Van Beek model [24], uses (1) for a prolate spheroid case with approximate N_j values and provides a final expression for calculating ε_{eff_z} given by (9):

$$\varepsilon_{eff_z} = \varepsilon_2 + \frac{f}{3} \frac{(\varepsilon_1 - \varepsilon_2)(5\varepsilon_2 + \varepsilon_1)}{\varepsilon_2 + \varepsilon_1} \tag{9}$$

Another famous formulation, known as Rayleigh's model for finding ε_{eff} in the direction perpendicular to the cylinder axes ($\varepsilon_{eff_{x,y}}$) is given by (10) [27]:

$$\varepsilon_{eff_{x,y}} = \varepsilon_2 \frac{\varepsilon_1 + \varepsilon_2 + f(\varepsilon_1 - \varepsilon_2)}{\varepsilon_1 + \varepsilon_2 - f(\varepsilon_1 - \varepsilon_2)} \tag{10}$$

The approximate value of $N_z = 1/2$ for a cylindrical particle in the z-direction is given by Kittel model [28]. To obtain the most accurate results, this value is optimized slightly. It should be noted that all the mixing rules that exist so far, have certain limitations, either in terms of the fractional volume or the particle geometry. There is no single formulation that works best for any particle's shape or any fractional volume. However, some of these models provide a good starting point, and then after some optimization, close agreement between the simulated and analytical results can be obtained.

III. EFFECTIVE PERMITTIVITY ANALYSIS

This section shows the complete analysis for finding the ε_{eff} of both isotropic (spherical) and anistropic (cylindrical) particles. Moreover, for each particle, two cases: conventional and complementary are considered. In a conventional case, the particle's permittivity ($\varepsilon_1 = 3.66$) is considered greater than the host permittivity ($\varepsilon_2 = 1$), i.e. $\varepsilon_1 > \varepsilon_2$. For the complementary case, the particle's permittivity ($\varepsilon_1 = 1$) is set lower than the host permittivity ($\varepsilon_2 = 3.66$), i.e. $\varepsilon_1 < \varepsilon_2$.

A. ISOTROPIC PARTICLE

Figures. 2(a) and (b) show the unit cell geometries for the conventional and complementary isotropic particles, respectively. The dimensions of the unit cell (length (l), width (w), and height (h) are chosen as: $l = w = h = \lambda_g/10 = 4.5$ mm, at a frequency of 3.5 GHz, where λ_g is the guided wavelength given as: $\lambda_g = \lambda_o/\sqrt{\epsilon_r}$, and λ_o is the free-space wavelength. a is the radius of the sphere. As the particle has a full symmetry, the ε_{eff} remains the same irrespective of the direction of excitation as well as irrespective of the polarization of the incident field ($\parallel$ or $\perp$). The fractional volume f of the spherical particle inside the host medium can be calculated as:

$$f = \frac{4\pi a^3}{3lwh} \tag{11}$$

Different values of f are obtained by varying a. The range of f is given as: $f_{min} = 0$ (no particle inside), $f_{max} : a = (l = w = h)/2$ (touching condition).

Figures. 2(c) and (e) show the simulated and calculated (using Eq. 2) ε_{eff} curves for the conventional and complementary cases, respectively. Figs. 2(d) and (f) show the % error for both cases. It can be seen that the results are in very good agreement with an overall error of < 2% for the whole range of f. Also, it can be observed that the % error starts increasing for the large values of f. This is one of the widely discussed limitations of the Maxwell Garnet mixing rule (1) and (2).

The other limitation of these formulations is in terms of the difference (Δ) between ε_1 and ε_2. This is shown in Fig. 3, where it can be seen that by increasing the particle's permittivity ε_1 from 2 to 10, while $\varepsilon_2 = 1$, the calculated results start diverging from the simulation ones. However, for the small values of f, a good agreement can be noticed. This analysis shows that the Maxwell Garnett mixing rule can be still be used for large Δ only by considering very small values of f.

B. ANISOTROPIC PARTICLE

1) ε_{eff} IN THE z-DIRECTION

Conventional Particle: To find the ε_{eff} in the z-direction (ε_{eff_z}), consider a cylindrical particle having

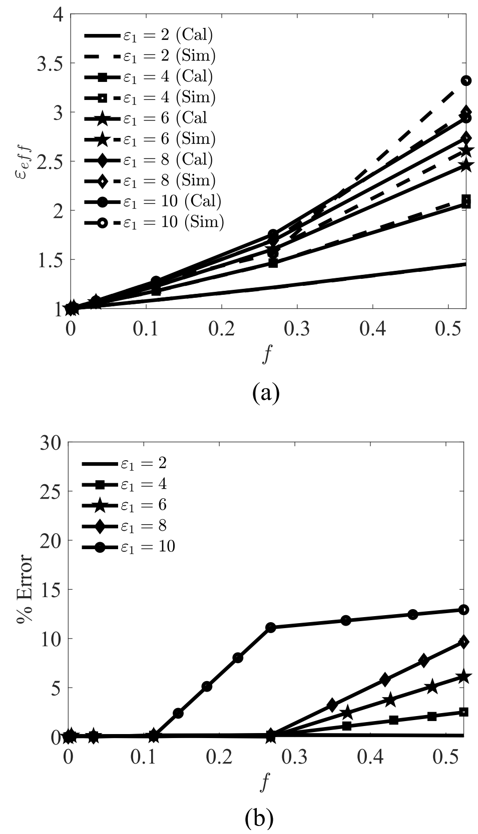

FIGURE 3. Limitation of Maxwell Garnett (2) [19]. (a) Comparison of the simulated and calculated ε_{eff} for different values of ε_1 when $\varepsilon_2 = 1$. (b) Permittivity perceptual error (%) as a function of f.

$\varepsilon_1 = 3.66$ (RO4350B), embedded in the host medium of $\varepsilon_2 = 1$ as shown in Fig. 4(a). The dimensions of the unit cell (l, w, and h) are chosen as: $l = w = \lambda_g/10$, and $h = 2.97$ mm, at a frequency of 3.5 GHz. H is the height of the particle, $H = h$. The particle is excited in the z-direction using Floquet ports with Master & Slave boundaries in HFSS^{TM}. As the direction of propagation (K_z) is parallel to the axis of the cylinder, the polarization of the incident E-field ($\parallel$ or $\perp$) does not affect the ε_{eff} due to the symmetry of the structure. The fractional volume f of the particle is given as:

$$f = \frac{\pi a^2 H}{4lwh} = \frac{\pi a^2}{4lw} \tag{12}$$

where a is the diameter of the cylinder. Figure 4(c) shows the comparison of the models with the simulation results for ε_{eff_z}, considering a conventional particle, and Fig. 4(d) shows the % error. It can be seen that the value: $N_z = 1/2$ from the Kittel model is in good agreement with the simulation results with an error of < 5% for the whole range of f.

Complementary Particle: Fig. 4(b) shows the unit cell geometry of the complementary cylinder particle having $\varepsilon_1 = 1$ inside a host medium having $\varepsilon_2 = 3.66$. The complementary particle having $\varepsilon_1 = 1$ is represented by a perforation (a through-drill where $H = h$). Figs. 4(e) and 4(f) show the ε_{eff} and % error, respectively, for the complementary

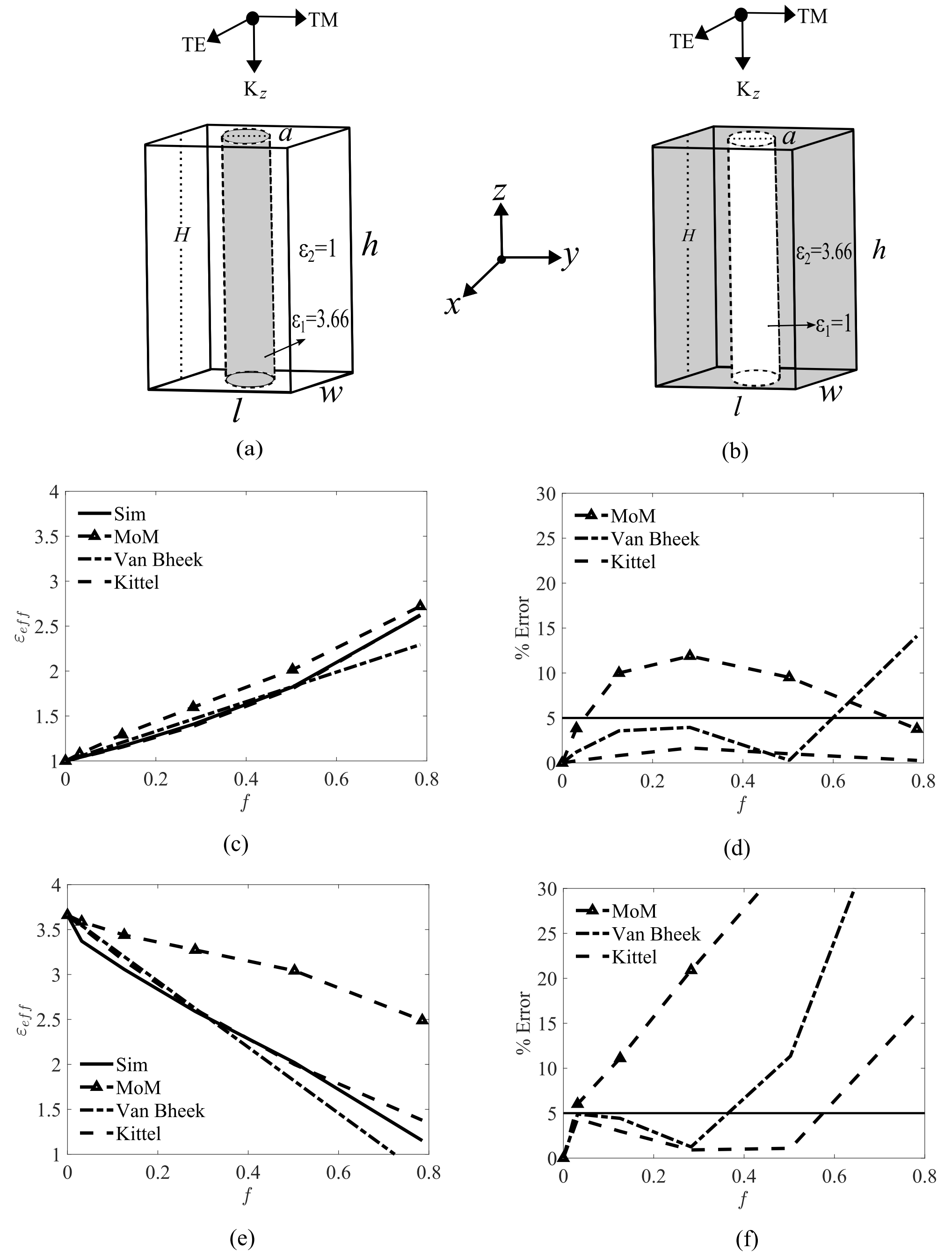

FIGURE 4. Permittivity analysis for the cylindrical particle excited in the z-direction. (a) Unit cell geometry of the conventional particle. (b) Unit cell geometry of the complementary particle. (c) Comparison of the models: MoM (6) [25], Van Bheek (9) [24], Kittel ($N_z = 1/2$) [28], with the simulation results, for the conventional particle. (d) Permittivity perceptual error (%) in the models for the conventional particle. (e) Comparison of the models: MoM (6) [25], Van Bheek (9) [24], Kittel ($N_z = 1/1.85$), with the simulation results, for the complementary particle. (f) Permittivity perceptual error (%) in the models for the complementary particle.

particle. It can be seen that for a very small value of $f < 0.03$, the models show good agreement. However, for the large values of f, the MoM model presents a significant departure as compared to the other two models. This is because the α_j values in MoM model were calculated for $\varepsilon_1 > \varepsilon_2$. The N_z value given in the kittel model is slightly tunned to $N_z = 1/1.85$ to get an error of $< 5\%$ for around 58% of f.

2) ε_{eff} IN THE x-, y-DIRECTIONS

To evaluate the ε_{eff} in x- or y-direction, it is important to note that the particle is symmetric in both x- and y-directions, therefore, $\varepsilon_{eff_x} = \varepsilon_{eff_y}$. However, the polarization of the incident field: $\mathbf{E}_\parallel$ or $\mathbf{E}_\perp$ as shown in Fig. 5, has an impact on the polarization field created inside the particle, which ultimately affects the ε_{eff}. Hence, the $\varepsilon_{eff_\parallel}$ and $\varepsilon_{eff_\perp}$ are

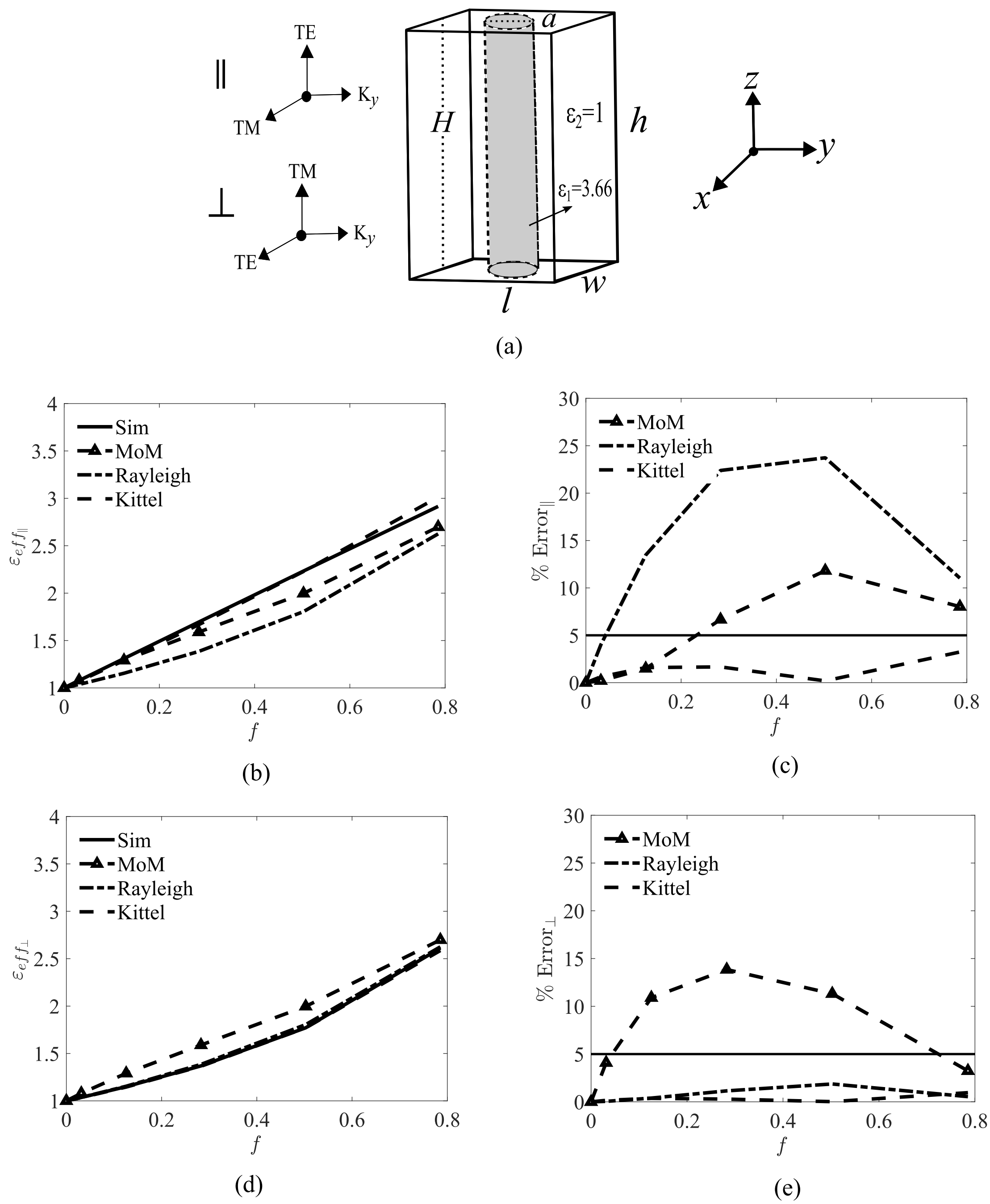

FIGURE 5. Permittivity analysis for the conventional particle excited in the x-, y-directions. (a) Unit cell geometry of the conventional particle. (b) Comparison of the models: MoM (7) [26], Rayleigh (10) [27], Kittel ($N_z = 1/15$), for $\varepsilon_{eff_{\parallel}}$. (c) Permittivity perceptual error (%) error in the models for $\varepsilon_{eff_{\parallel}}$. (d) Comparison of the models: MoM (7) [26], Rayleigh (10) [27], Kittel ($N_z = 1/1.8$), for $\varepsilon_{eff_{\perp}}$. (e) Permittivity perceptual error (%) in the models for $\varepsilon_{eff_{\perp}}$.

evaluated separately, for both conventional and complementary cases.

Conventional Particle: Fig. 5 shows the geometry of the conventional particle as well as the comparison of the models for both $\parallel$ and $\perp$ polarizations. It can be seen that the MoM model presents a minimum of 10% error for both cases. The Rayleigh model shows a comparatively large deviation in the $\parallel$ case while its error is < 5% for the whole f, in the $\perp$ case. The initial value of $N_z = 1/2$ provided by the Kittel model is tunned to have an error of < 5% for both cases. This analysis shows the sensitivity of ε_{eff} to the polarization of the incident field.

Complementary Particle: Fig. 6 shows the geometry of the complementary particle and the ε_{eff} analysis for both $\parallel$ and $\perp$ polarizations. It can be seen that, as expected the MoM models show significant deviation from the simulation results for both $\parallel$ and $\perp$ cases. The Rayleigh model shows a maximum of 12% error for the $\parallel$ case while it converges well

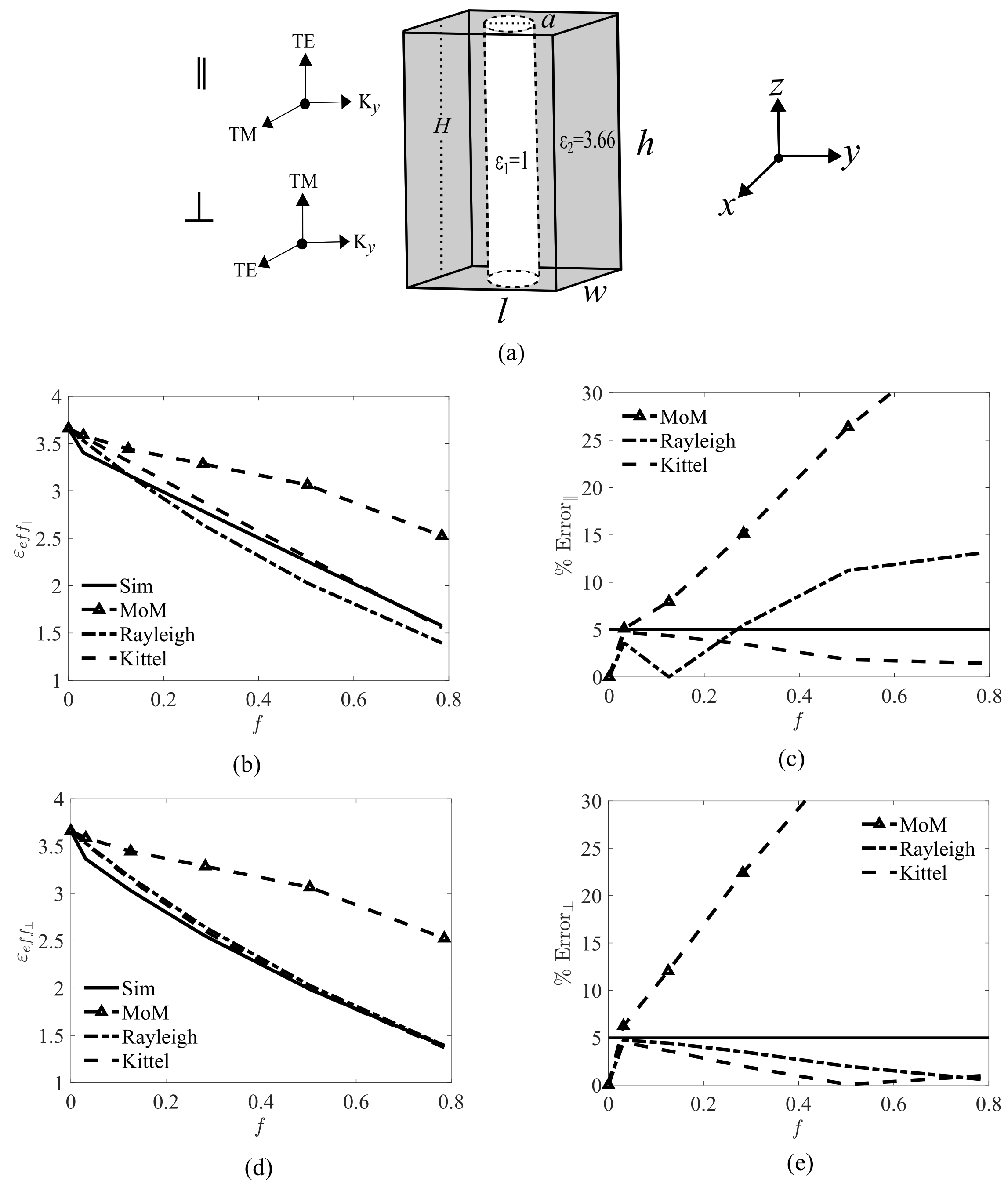

FIGURE 6. Permittivity analysis for the complementary particle excited in the x-, y-directions. (a) Unit cell geometry of the complementary particle. (b) Comparison of the models: MoM (7) [26], Rayleigh (10) [27], Kittel ($N_z = 1/20$), for $\varepsilon_{eff_\parallel}$. (c) Permittivity perceptual error (%) error in the models for $\varepsilon_{eff_\parallel}$. (d) Comparison of the models: MoM (7) [26], Rayleigh (10) [27], Kittel ($N_z = 1/1.8$), for $\varepsilon_{eff_\perp}$. (e) Permittivity perceptual error (%) in the models for $\varepsilon_{eff_\perp}$.

for the $\perp$ case with an error of $< 5\%$ for the whole f. The values of N_z in the Kittel model are tunned for both cases to have an error of $< 5\%$.

IV. MATERIAL DESIGN AND SYNTHESIS

A. MATERIAL REQUIREMENTS

Among the several critical parameters discussed in the introductory section for choosing the right material for both microwave and mm-Wave applications, the ε_r and the material's dielectric loss or tanδ are of significant importance. As compared to the microwave frequencies, where a high ε_r can be used, at mm-Wave frequencies, a low ε_r material is highly recommended, because using a high ε_r material would further reduce the size of the structure thus creating more challenges in the fabrication [29]. Also, the losses in the material are often related to the value of ε_r. Higher the value of ε_r, higher are the losses in the material [29]. Therefore, at mm-Wave frequencies where the losses are significant, a low ε_r material is used to reduce further losses in the material. Moreover, at high frequencies, the speed of signal propagation in the high-speed circuits is very important. The signal propagation delay (t_d) depends on both the guiding structure as well as on the ε_r of the material and is given by 13 [12]:

$$t_d = \sqrt{\varepsilon_r \times L \times C} \tag{13}$$

where L and C are the inductance and capacitance of the line. Eq. (13) shows that by using a low ε_r material or different transmission line structures (microstrip, stripline or coplanar waveguide, etc.), t_d can be directly reduced. Cross-talk is also of utmost consideration when referring to mm-Wave frequencies. Using a low ε_r material in the high-frequency circuits can decrease the capacitive coupling between the conductors and thus cross-talk can be reduced [12]. Aside from the values of ε_r, more important is the consistency of the ε_r at mm-Wave frequencies. A slight variation in material ε_r can cause a change in the impedance of the transmission line which can cause unexpected variations in the phase angles resulting in errors in radar signal detection [11].

Another important property of the material is the tanδ. At both microwave and mm-Wave frequencies, dielectrics with low losses are used to reduce attenuation and heating in the circuit [12]. Current substrate materials have the tanδ values between $0.002 < \tan\delta < 0.02$. However, At the mm-Wave frequencies, the requirements become more stringent and tanδ values of < 0.002 are desired [29].

B. DESIGN TRADE-OFFS

As compared to other particles discussed in Sec. III, the complementary cylindrical particles inside a host medium which are commonly known as air perforations, offer several advantages in terms of easiness in fabrication (can be easily drilled) and measurement, reduce complexity in modeling the depolarization field due to its perfect alignment inside the structure, and help in reduction of the loss tangent of the material. The air perforations in the host material with $\varepsilon_1 \approx 1$ and a $\tan\delta \approx 0$, has a very useful feature of reducing the overall

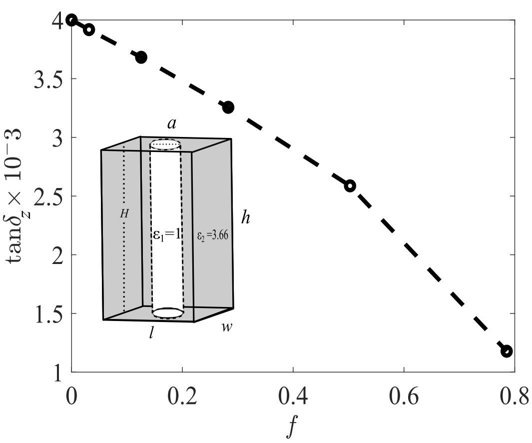

FIGURE 7. Reduction in the overall loss tangent of the material based on different values of *f*.

tanδ. Fig. 7 shows the reduction in the loss tangent of the host material by using a complementary cylindrical particle. It can be seen that when there is no particle inside i.e. $f = 0$, the original value of $\tan\delta = 0.004$ (RO4350B). However, for the maximum value of $f = 0.78$, the value of $\tan\delta = 0.0012$, which shows a reduction of around 70% in the tanδ of the core-material.

C. DESIGN PROCEDURE

Figure. 8 shows the simulation setup for the unit cell geometry of the proposed material structure using an infinite array approach in HFSS^{TM}. The required Floquet ports along with the Master and Slave boundaries are used. In this case, the material is excited in the z-direction with two de-embedded ports. The real and imaginary parts of the S-parameters are used to extract the constitutive parameters (ε_{eff}, μ_r, tanδ) by using the Smith algorithm [30].

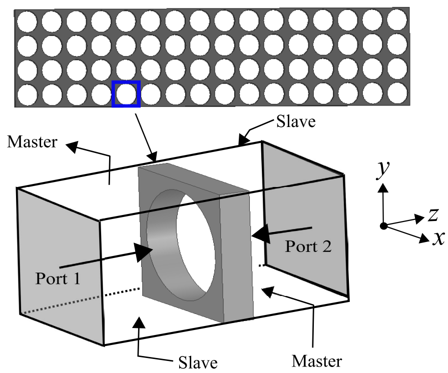

FIGURE 8. Simulation setup showing the unit cell geometry of the periodic structure with Floquet ports excitation and boundaries.

D. SIZE OF THE UNIT CELL

Determining the size of the unit cell of the periodic structure in terms of the wavelength is critical for extracting the correct values of the constitutive parameters [31]. For this the particle should meet the effective-homogeneity condition which is when the size of the unit cell is $< \lambda_g/4$ [31]. Moreover, a slight change in the value of ε_r over the range of frequencies can degrade the performance specifically at mm-Wave frequencies. Fig. 9 shows the effect of the size of the unit cell on the ε_{eff} and tanδ over the range of frequencies, for z- and x-, y-directions. For the purpose of illustration, a cubic unit cell of a complementary cylindrical particle excited in the z- and x- or y-directions is considered with $f = 56\%$. Different dimensions of the unit cell are considered in terms of the λ_g at the highest frequency of operation i.e. 40 GHz. The cases considered have the dimensions $\leq 0.5\lambda_g$, because, for the size of the unit cell greater than $0.5\lambda_g$, no convergence was observed. For comparison, f should remain the same for all the cases. Therefore, for each case, the diameter of the cylinder is adjusted to get the same values of f.

Figures. 9(a) and (b) show the ε_{eff} and the tanδ in the z-direction. Fig. 9(a) shows the difference in the values of ε_{eff_z}

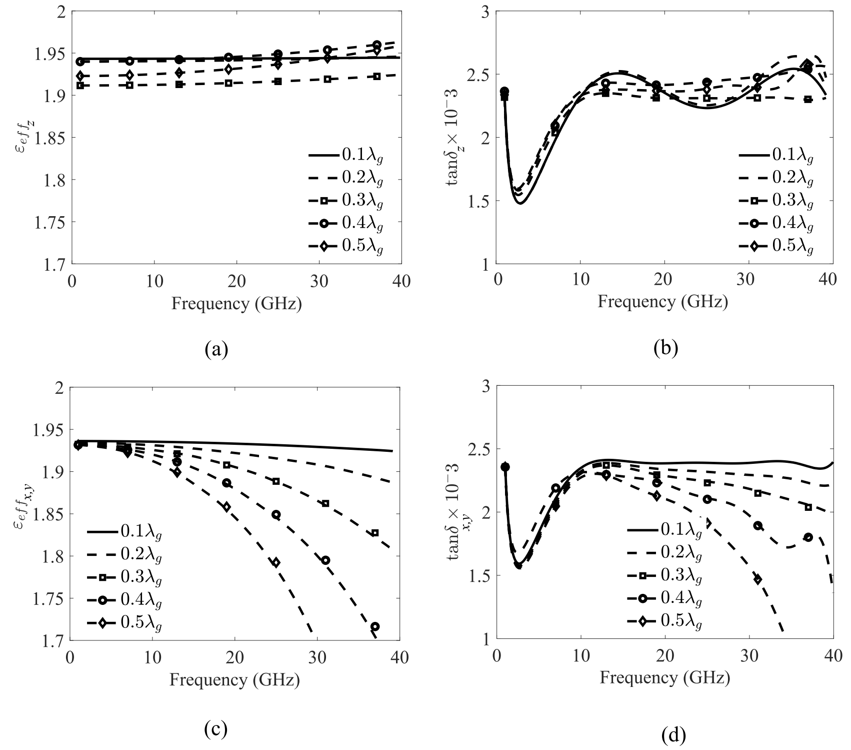

FIGURE 9. ε_{eff} and tanδ as function of the unit cell dimensions for the complementary cylindrical particle using 4350B with perforation. (a) ε_{eff} in the z-direction. (b) tanδ in the z-direction. (c) ε_{eff} in the x-, y-directions. (d) tanδ in the x-, y-directions.

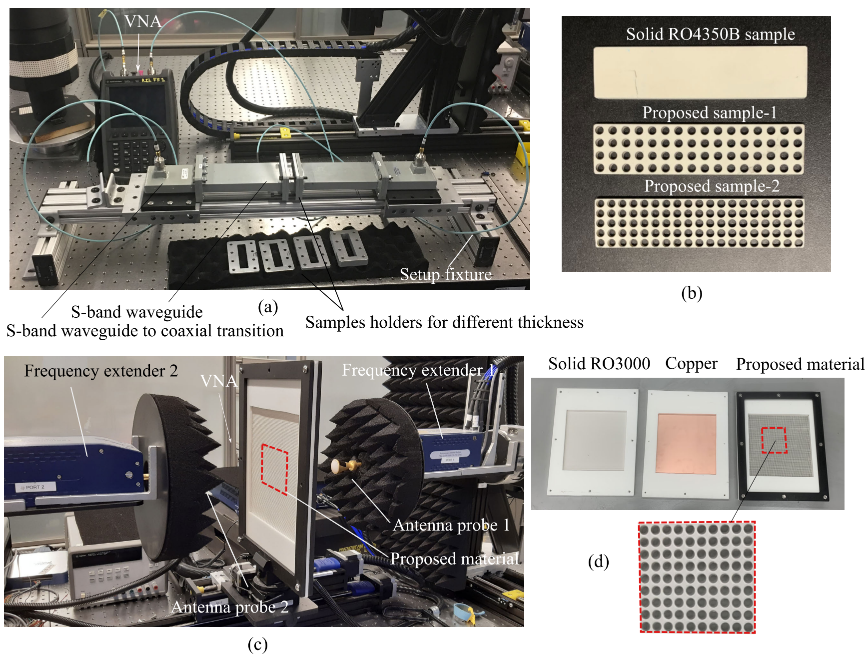

FIGURE 10. Material measurement setups for low and high frequencies. (a) Photo of the measurement setup for S-band, based on the waveguide method. (b) Material samples used for the S-band test. (c) Photo of the measurement setup for W-band, based on the free-space Gaussian beam method. (d) Material samples used for W-band test.

at lower frequencies as well as an increasing trend at higher frequencies for different dimensions of the unit cell. However, for the case of $0.1\lambda_g$, the values of ε_{eff_z} are stable over the entire frequency range. Figs. 9(c) and (d) show this analysis for the x-, y-directions. It can be seen that for the unit cell size of $0.1\lambda_g$, stable performance is obtained. However, when the

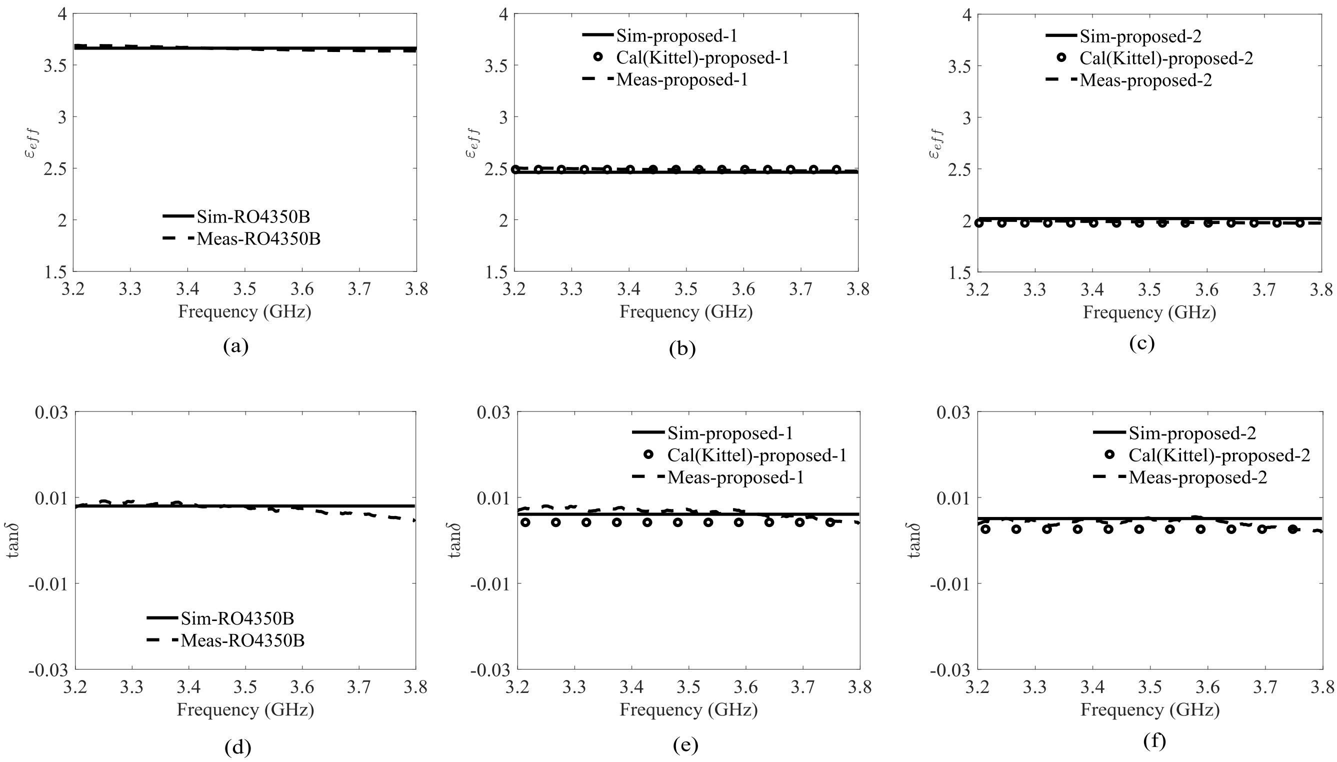

FIGURE 11. Comparison between measured, simulated, and calculated results in the S-band. (a) ε_{eff} solid sample (RO4350B). (b) ε_{eff} proposed sample-1.(c) ε_{eff} proposed sample-2 with Kittel ($N_z = 1/2.4$). (d) tanδ solid RO4350B sample. (e) tanδ proposed sample-1 with Kittel ($N_z = 1/2.8$). (f) tanδ proposed sample-2 with Kittel ($N_z = 1/2.4$).

TABLE 1. Summary of ε_{eff} and tanδ for x-, y-, and z-directions for solid and proposed material for 1 GHz to 40 GHz.

	Freq. (GHz)	Size (λ_g^3)	Results								
			Parameters					Reduction factor			
			f	$\varepsilon_{eff_{x,y}}$	ε_{eff_z}	tan$\delta_{x,y}$	tanδ_z	$\varepsilon_{eff_{x,y}}$	ε_{eff_z}	tan$\delta_{x,y}$	tanδ_z
Solid Reference 4350B	40	$0.1\lambda_g$	–	3.66	3.66	0.004	0.004	–	–	–	–
Proposed	40	$0.1\lambda_g$	0.56	1.92	1.95	0.0022	0.0024	47.5%	46.7%	45%	40%

size gets larger, a decreasing trend can be observed. From this, it can be concluded that in order to have a steady performance in terms of ε_{eff_z} or $\varepsilon_{eff_{x,y}}$, the z- or x-, y-dimensions of the unit cell should be at least $\leq 0.1\lambda_g$ at the higher frequency of operation. Smaller the size of the unit cell, the more stable is the performance. However, fabrication tolerances should be considered while determining the size of the unit cell.

The results from this analysis are summarized in Table 1. The dimensions of the unit cell are $0.1\lambda_g$ at 40 GHz. As the reference RO4350B sample is isotropic, the values of ε_{eff} and tanδ for any direction are the same given in the data sheet. However, for the proposed sample loaded with anisotropic complementary cylindrical particle, the values of ε_{eff} and tanδ slightly differ between the x-, y-, and z-directions. The reason for this has been explained in detail in Sec. III.

For determining the size of the unit cell for the W-band, the same unit cell size analysis was carried out at 77 GHz, using solid RO3003 as the reference sample. The dimensions of the unit cell were chosen based on the stable performance as well as keeping the fabrication tolerances in consideration. As the permittivity is measured in the z-direction, for sample-3 the z-dimension or thickness H of the material, which is more sensitive to the performance, was chosen to be small as $0.226\lambda_g$ at 77 GHz in order to achieve accurate and stable results. The other dimensions of the unit cell were kept comparatively larger as $1\lambda_g$ due to fabrication restrictions.

V. MEASUREMENT RESULTS AND VALIDATION

To validate the analysis presented before, two different samples were fabricated and measured in the S-band at 3.5 GHz and a third sample in the mm-Wave W-band at 77 GHz. The proposed samples were designed using the analysis presented in Sec. II-IV. These samples were fabricated using LPKF Protomat S103 machine and were measured using the setups shown in Fig.10. The ε_{eff} of the S-band samples: sample-1 and sample-2 were measured using the waveguide setup of Fig. 10(a), and the W-band sample-3 was characterized using the mm-Wave RF scanner shown in Fig. 10(c).

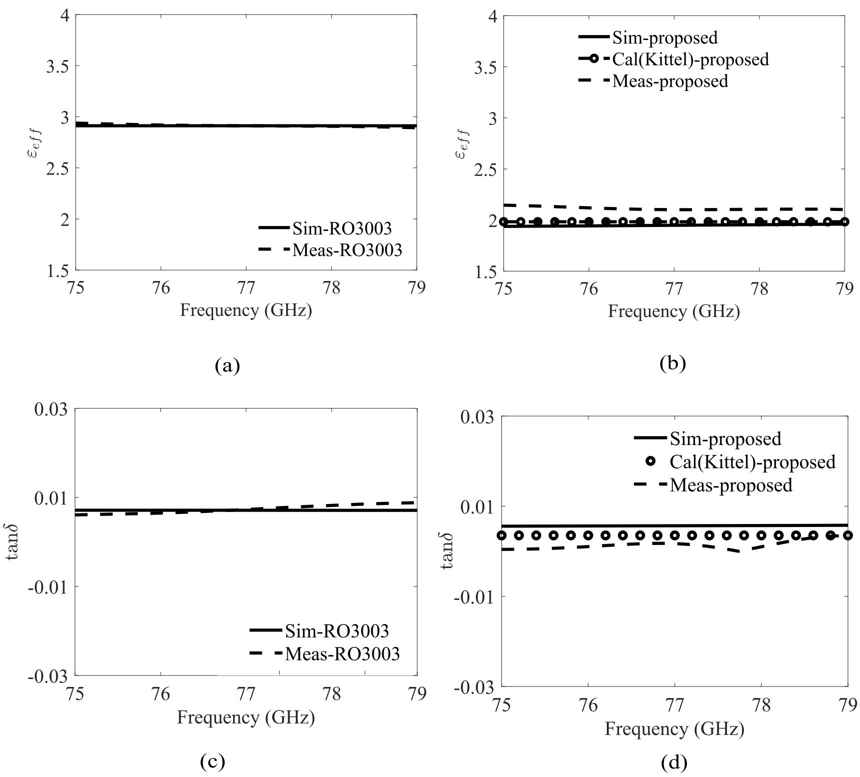

FIGURE 12. Comparison between measured, simulated, and calculated (Kittel model $N_z = 1/30$) results in W-band. (a) ε_{eff} solid sample (RO3003). (b) ε_{eff} proposed sample-3. (c) tanδ solid sample (RO3003). (d) tanδ proposed sample-3.

TABLE 2. Summary of the measured results of ε_{eff} and tanδ in the z-direction for solid and proposed material in the S-band and W-band.

	Material	Freq. (GHz)	Size (mm)					Results				
								Parameters			Reduction factor	
			l	w	h	H	a	f	ε_{eff_z}	$tan\delta_z$	ε_{eff_z}	$tan\delta_z$
Reference	RO4350B	3.5	–	–	–	2.97	–	–	3.66	0.008	–	–
Sample-1	RO4350B	3.5	4.51	4.25	2.97	2.97	3	0.37	2.46	0.006	33%	25%
Sample-2	RO4350B	3.5	3.8	3.40	2.97	2.97	3	0.55	2	0.005	45%	38%
Reference	RO3003	77	–	–	–	0.508	–	–	2.91	0.0072	–	–
Sample-3	RO3003	77	2.25	2.25	0.508	0.508	1.8	0.5	1.98	0.002	32%	72%

TABLE 3. Performance comparison of the proposed work with other related works.

References	Theory & modeling	Design procedure	Particle geometry	Polarization & excitation analysis	Error analysis	Application	Freq. (GHz)
[4]	*	*	Cylindrical	*	*	SIIG	94
[5]	*	*	Cylindrical	*	*	SIIG	94
[6]	*	*	Cylindrical	*	*	SIIG	94
[7]	Yes	Yes	Cylindrical	*	*	Reconfigurablility	4.2-4.9
[8]	*	*	Cylindrical	*	*	mm-Wave imaging	94
[9]	*	*	Cylindrical	*	*	mm-Wave	100
This work	Yes	Yes	Any isotropic or anisotropic	Yes	Yes	Any	1-110

* Not discussed in the paper.

The measurement results were compared with the reference samples. The simulated, calculated, and measured results in terms of ε_{eff_z} and tanδ are shown in Fig. 11 for the S-band samples, and in Fig. 12 for the W-band sample-3. Fig. 10(b) and (d) shows the reference and the proposed samples for the S-band and the W-band, respectively. For the S-band samples: sample-1 and sample-2, the dimensions of the unit cell are kept $\leq \lambda_g/10$ at 3.5 GHz based on the analysis presented in Sec. IV. The dimensions of the unit cell in both cases are varied to obtain different values of f. Figs. 11 and 12 show an excellent agreement between the simulated, calculated, and measured results. For sample-3, the thickness H of the material is chosen to be small as $0.226\lambda_g$ at 77 GHz in order to achieve accurate and stable results. The other dimensions of the unit cell are kept comparatively large due to fabrication challenges at 77 GHz. However, all the dimensions are tuned to get convergence in the results.

All the dimensions as well as the results for the S-band and the W-band samples are also summarized in Table 2. It should be noted that the measured value of the tanδ for the reference RO4350B sample given in the Table 2 is 0.008 and not 0.004 (from data sheet). Similarly, the values of ε_r and tanδ for the reference RO3003 sample are 2.91 and 0.0072, respectively, measured at 77 GHz. This variation in the results can be attributed to the selection of the measurement method, frequency of operation, external environmental conditions, and slight inaccuracy in the measurement setup. It should also be noted that each measured ε_{eff} curve in Fig. 11 or 12 represents the statistical average of several repeated measurements to ensure stability in the results and to reduce errors associated with the measurement. It can be seen that for sample-1 having $f = 37\%$, the reduction in ε_{eff_z} and tanδ is 33% and 25%, respectively. For sample-2 with $f = 55\%$, a reduction of 45% and 38% is obtained in the ε_{eff_z} and tanδ, respectively, as compared to the solid reference sample RO4350B shown in Fig. 11(a). Similarly, for sample-3 with $f = 50\%$, a reduction of 32% and 72% is achieved in the values of ε_{eff} and tanδ, respectively, as compared to the reference RO3003 sample shown in Fig. 12(a).

Table 3 shows the performance comparison of the proposed work with other related works. It can be noticed that as compared to other works, the proposed work validates the analytical models based on the error analysis and also discusses anisotropy of the material based on the direction of excitation and polarization analysis. Moreover, the proposed design procedures can be applied in the design of a high-performance material at any frequency between 1-110 GHz, for many applications.

VI. CONCLUSION

In this paper, a proposed method based on Maxwell Garnett mixing theory is used to obtain a high-performance RF material, from an existing high thermally stable and compatible material. A complete set of design equations for finding desirable ε_{eff} of both isotropic and anisotropic particles is presented. The permittivity analysis for both isotropic and anisotropic cases is thoroughly studied including the effects of the direction of excitation as well as polarization of the incident field on the ε_{eff}. Detailed design procedures and requirements are discussed for both microwave and mm-Wave applications. Several analytical models are discussed and evaluated for their performance. The most accurate model is identified and used to find the ε_{eff} of the anisotropic cylindrical particle in any direction of excitation as well as any polarization of the incident field. Building on all the advantages of the existing substrate materials, the proposed method can be used to obtain the desired lower ε_r and tanδ values. Thus, enabling the use of inexpensive materials to be used as high-performance RF substrates for applications that require high antenna efficiency, multi-layer PCB compatibility, and high thermal stability. For the proof of concept, samples were fabricated and tested in the S-band at 3.5 GHz as well as in the W-band at 77 GHz. A reduction of 45% in the ε_{eff} and 38% in the loss tangent values was obtained in the S-band, and 32% and 72% reduction in ε_{eff} and tanδ, respectively, in the W-band. Excellent agreement was obtained between the simulation, calculated, and measured results.

ACKNOWLEDGMENT

The authors would like to thank the Advanced Radar Research Center (ARRC) at The University of Oklahoma for providing the facilities needed to perform this research. The authors would also like to thank the members of the Phased Array Antenna Research and Development Group (PAARD) for the discussions and feedbacks. Special thanks to Alex Oblitas for developing the graphical user interface.

REFERENCES

[1] L. Tsang, J. A. Kong, and R. T. Shin, *Theory of Microwave Remote Sensing*. Washington, DC, USA: NASA, 1985.

[2] W. E. Kock, "Metal-lens antennas," *Proc. IRE*, vol. 34, no. 11, pp. 828–836, Nov. 1946.

[3] B. Sareni, L. Krähenbühl, A. Beroual, and C. Brosseau, "Effective dielectric constant of periodic composite materials," *J. Appl. Phys.*, vol. 80, no. 3, pp. 1688–1696, Aug. 1996.

[4] A. Patrovsky and K. Wu, "Substrate integrated image guide (SIIG)—A low-loss waveguide for millimetre-wave applications," in *Proc. Eur. Microw. Conf.*, vol. 2, Oct. 2005, p. 4.

[5] A. Patrovsky and K. Wu, "Substrate integrated image guide (SIIG)—A planar dielectric waveguide technology for millimeter-wave applications," *IEEE Trans. Microw. Theory Techn.*, vol. 54, no. 6, pp. 2872–2879, Jun. 2006.

[6] A. Patrovsky and K. Wu, "94-GHz planar dielectric rod antenna with substrate integrated image guide (SIIG) feeding," *IEEE Antennas Wireless Propag. Lett.*, vol. 5, pp. 435–437, 2006.

[7] J. L. Salazar-Cerreno, Z. Qamar, S. Saeedi, B. Weng, and H. S. Sigmarsson, "Frequency agile microstrip patch antenna using an anisotropic artificial dielectric layer (AADL): Modeling and design," *IEEE Access*, vol. 8, pp. 6398–6406, 2020.

[8] J. B. Muldavin and G. M. Rebeiz, "Millimeter-wave tapered-slot antennas on synthesized low permittivity substrates," *IEEE Trans. Antennas Propag.*, vol. 47, no. 8, pp. 1276–1280, Aug. 1999.

[9] P. Mondal and K. Wu, "A leaky-wave antenna using periodic dielectric perforation for millimeter-wave applications," *IEEE Trans. Antennas Propag.*, vol. 64, no. 12, pp. 5492–5495, Dec. 2016.

[10] M. T. Sebastian, R. Ubic, and H. Jantunen, *Microwave Materials and Applications*. Hoboken, NJ, USA: Wiley, 2017.

[11] J. Coonrod, "Choosing circuit materials for millimeter-wave applications," *High Freq. Electron.*, vol. 12, no. 7, pp. 22–30, 2013.

[12] M. D. Janezic, N. Paulter, and J. Blendell, "Dielectric and conductor-loss characterization and measurements on electronic packaging materials," NIST Tech. Note 1520, 2001.

[13] *A High Performance, Economical RF/Microwave Substrate*, Taconic, Advanced Dielectric Division, Petersburgh, NY, USA, 1998.

[14] J. C. M. Garnett, "XII. Colours in metal glasses and in metallic films," *Philos. Trans. Roy. Soc. London A, Containing Papers Math. Phys. Character*, vol. 203, nos. 359–371, pp. 385–420, Sep. 1904.

[15] D. Bruggeman, "Dielectric constant and conductivity of mixtures of isotropic materials," *Ann. Phys.*, vol. 24, pp. 636–679, Feb. 1935.

[16] H. Looyenga, "Dielectric constants of heterogeneous mixtures," *Physica*, vol. 31, no. 3, pp. 401–406, Mar. 1965.

[17] D. Polder and J. H. van Santeen, "The effective permeability of mixtures of solids," *Physica*, vol. 12, no. 5, pp. 257–271, Aug. 1946.

[18] K. Lichtenecker and K. Rother, "Deduction of the logarithmic mixture law from general principles," *Phys. Z*, vol. 32, pp. 255–260, 1931.

[19] A. H. Sihvola and J. A. Kong, "Effective permittivity of dielectric mixtures," *IEEE Trans. Geosci. Remote Sens.*, vol. 26, no. 4, pp. 420–429, Jul. 1988.

[20] A. H. Sihvola, "Mixing rules with complex dielectric coefficients," *Subsurface Sens. Technol. Appl.*, vol. 1, no. 4, pp. 393–415, 2000.

[21] L. Landau and E. Lifshitz, *Electrodynamics of Continuous Media*, 2nd ed. Oxford, U.K.: Pergamon press, 1984, sec. 4.

[22] J. A. Osborn, "Demagnetizing factors of the general ellipsoid," *Phys. Rev.*, vol. 67, nos. 11–12, p. 351, 1945.

[23] E. C. Stoner, "XCVII. The demagnetizing factors for ellipsoids," *London, Edinburgh, Dublin Phil. Mag. J. Sci.*, vol. 36, no. 263, pp. 803–821, Dec. 1945.

[24] L. Van Beek, *Progress in Dielectrics*, vol. 7. Heywood, U.K., 1967, p. 69.

[25] A. Sihvola, J. Venermo, and P. Ylä-Oijala, "Dielectric response of matter with cubic, circular-cylindrical, and spherical microstructure," *Microw. Opt. Technol. Lett.*, vol. 41, no. 4, pp. 245–248, May 2004.

[26] A. H. Sihvola, P. Yla-Oijala, S. Jarvenpaa, and J. Avelin, "Polarizabilities of platonic solids," *IEEE Trans. Antennas Propag.*, vol. 52, no. 9, pp. 2226–2233, Sep. 2004.

[27] J. W. Rayleigh, "On the influence of obstacles arranged in rectangular order upon the properties of a medium," *Philos. Mag.*, vol. 34, no. 211, pp. 481–502, 1892.

[28] C. Kittel, *Introduction to Solid State Physics*, 8th ed. New York, NY, USA: Wiley, 2004.

[29] J. Coonrod, "Selecting circuit material for the different spectra of 5G power amplifiers," *Microw. J. E-Book*, pp. 18–21, Feb. 2018.

[30] D. R. Smith, W. J. Padilla, D. C. Vier, S. C. Nemat-Nesser, and S. Schultz, "Composite medium with simultaneously negative permeability and permittivity," *Phys. Rev. Lett.*, vol. 84, p. 4184, May 2000.

[31] C. Caloz and T. Itoh, *Electromagnetic Metamaterials: Transmission Line Theory and Microwave Applications*. Hoboken, NJ, USA: Wiley, 2005.

SYED SHAHAN JEHANGIR received the B.S. degree in electrical (telecommunication) engineering from the COMSATS Institute of Information Technology, Lahore, Pakistan, in 2014, and the M.Sc. degree in electrical engineering from the King Fahd University of Petroleum and Minerals (KFUPM), Dhahran, Saudi Arabia, in 2017. In 2014, he was a Research Assistant with the School of Electrical Engineering and Computer Science, National University of Science and Technology (NUST), Islamabad, Pakistan. From 2017 to 2019, he was a Research Associate with the Department of Electrical Engineering, United Arab Emirates University, Al-Ain, United Arab Emirates. He is currently a Graduate Research Assistant (GRA) with the Advanced Radar Research Center (ARRC), Phased Array Antenna Research and Development (PAARD) Group, The University of Oklahoma (OU), USA. He has published more than 20 refereed journal and conference papers. His research interests include phased array antennas for radar applications, lens antennas for mm-wave automotive radars, material characterization, directional and miniaturized MIMO antennas for 4G/5G, and reconfigurable MIMO antennas. He received the Campus Gold Medal for securing the highest cumulative GPA in his batch during the undergraduate studies.

ZEESHAN QAMAR (Member, IEEE) received the B.Sc. and M.Sc. degrees in electrical engineering from COMSATS University, Islamabad, Pakistan, in 2010 and 2013, respectively, and the Ph.D. degree in electronic engineering from the City University of Hong Kong, Hong Kong, in 2017. From July 2010 to August 2013, he was a Research Associate with the Department of Electrical and Computer Engineering, COMSATS University. From November 2017 to April 2018, he was a Postdoctoral Research Associate with the Department of Materials Science and Engineering, City University of Hong Kong. He is currently a Postdoctoral Research Fellow with the Phased Array Antenna Research and Development (PAARD) Group and the Advanced Radar Research Center (ARRC), The University of Oklahoma, Norman, OK, USA. His current research interests include microwave/millimeter-wave circuits, material characterization, meta-materials, artificial dielectric layer, antennas, phased arrays, and phased array antennas. He is a member of the IEEE Antennas and Propagation Society (AP-S). He serves as a Reviewer for various the IEEE and IET conferences and journals.

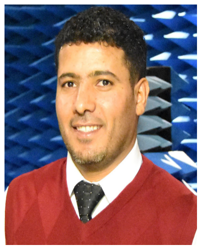

NAFATI ABOSERWAL (Member, IEEE) received the B.S. degree in electrical engineering from Al-Mergheb University, Al-khums, Libya, in 2002, and the M.S. and Ph.D. degrees in electrical engineering from Arizona State University, Tempe, AZ, USA, in 2012 and 2014, respectively. In January 2015, he joined the Advanced Radar Research Center (ARRC) and the Department of Electrical and Computer Engineering, The University of Oklahoma (OU), Norman, as a Postdoctoral Research Scientist. He is currently a Research Associate and a Manager with the Far-Field, Near-Field, and Environmental Anechoic Chambers, Radar Innovations Laboratory (RIL). His research interests include EM theory, computational electromagnetics, antennas, diffraction theory, edge diffraction, discontinuities impact on the array performance, active high-performance phased array antennas for weather radars, higher-modes, surface waves characteristics of printed antennas, and high-performance dual-polarized microstrip antenna elements with low-cross-polarization. He is a member of the IEEE Transactions on Antennas and Propagation.

JORGE L. SALAZAR-CERRENO (Senior Member, IEEE) received the B.S. degree in ECE from Antenor Orrego Private University, Trujillo, Peru, the M.S. degree in ECE from the University of Puerto Rico, Mayagüez (UPRM), and the Ph.D. degree in ECE from the University of Massachusetts, Amherst, MA, USA, in 2011. His Ph.D. research was on development of low-cost dual-polarized active phased array antennas (APAA). At NCAR, he was with the Earth Observing Laboratory (EOL) Division, developing airborne technology for two-dimensional, electronically scanned, and dual-pol phased array radars for atmospheric research. In July 2014, he joined the Advanced Radar Research Center (ARRC), The University of Oklahoma, as a Research Scientist. He was an Assistant Professor with the School of Electrical and Computer Engineering in August 2015. His research interests include high-performance, broadband antennas for dual-polarized phased array radar applications, array antenna architecture for reconfigurable radar systems, APAA, Tx/Rx modules, radome EM modeling, and millimeter-wave antennas. He is a Senior Member of the IEEE Antennas and Propagation Society (AP-S). He received the Prestigious National Center for Atmospheric Research (NCAR) Advanced Study Program (ASP) Postdoctoral Fellowship and the Prestigious William H. Barkow Presidential Professorship from The University of Oklahoma for meeting the highest standards of excellence in scholarship and teaching in 2019. He serves as a Reviewer for various the IEEE and AMS conferences and journals.